PNAS

www.pnas.org

Supplementary Information for

Electrochemical removal of amphoteric ions

Amit N. Shocron, Eric N. Guyes, Huub H.M. Rijnaarts, P.M. Biesheuvel, Matthew E. Suss and Jouke E. Dykstra

Matthew E. Suss
E-mail: mesuss@me.technion.ac.il
Jouke E. Dykstra
E-mail: jouke.dykstra@wur.nl

This PDF file includes:

Supporting Information Text

Experimental values of boron electrosorption, Γ_B, and feed pH, pH_F, used in this study are reported in Table S1.

S1. High charging voltage results in a local pH minimum

As presented in Fig. 3A of the main article, for the highest charging voltage investigated, $V_{ch} = 1.4$ V, a pH minimum develops in the downstream electrode (cathode). As explained in the main article, we hypothesize the development of a low pH minimum is related to very low values of macropore Na$^+$ concentration, c_{mA,Na^+}, in the cathode. Here, we extend our analysis and present further results. Fig. S1A presents profiles of pH (left y axis, black lines) and c_{mA,Na^+} on a logarithmic scale (right y axis, blue lines) for V_{ch}=1.0 V (dashed lines) and 1.4 V (dotted lines), at t/τ_D=2, both with Péclet number, Pe, of 3 and feed salt concentration, c_F, of 2 mM.

The pH profiles in Fig. S1A are the same profiles presented in the main article, including low pH values in most of the anode, followed by a strong increase near the anode/separator interface, and relatively high values in the separator and the anode. However, local pH minima develop in the cathode, where the minimum for V_{ch}=1.4 V is much more locally confined to a narrow region with lower pH. By observing c_{mA,Na^+} on a logarithmic scale, we observe the locations of c_{mA,Na^+} minima for both V_{ch}=1.0 V and 1.4 V coincides with the locations of the pH minima. Moreover, the c_{mA,Na^+} minimum for V_{ch}=1.4 V is much lower than at other voltages. Overall, the results presented in Fig. S1A support our hypothesis that the development of local pH minimum is related to very low c_{mA,Na^+} in the cathode.

The relation between very low c_{mA,Na^+} values and the pH minimum is also found in Fig. S1B, a spatiotemporal presentation of c_{mA,Na^+} on a logarithmic scale. Across most of the cell, $c_{mA,Na^+} \geq 10^{-2}$ mM, while a thin region of extremely low concentrations (10^{-6} mM $\leq c_{mA,Na^+} \leq 10^{-3}$ mM) develops near the cathode/separator interface at $t/\tau_D \approx 1$, slowly propagating downstream. This feature coincides with the pH minimum, developing at the same locations and times, as presented in Fig. 3D in the main article. Overall, Fig. S1B supports the observation there is a relation between the occurrence of a pH minimum in the cathode and very low values of c_{mA,Na^+}.

S2. Electrodes and separator thickness analysis

In this section we present our analysis of how the electrodes and separator thickness affect pH and boron concentration dynamics.

S2.1. Separator thickness analysis. In Fig. S2 we present characteristic results for different values of the separator thickness, l_{sep}, where we analyze a theoretical cell with the parameters presented in Table 1 and in column 3 of Table 2 of the main article. Fig. S2A, C and E present the profiles of pH (left y axes, black lines) and macropore salt concentration (right y axes, blue lines), and Fig. S2B, D and F present profiles of dimensionless potential, ϕ (left y axes, black lines), and macropore B$^-$ concentration (right y axes, blue lines), all at t/τ_D=2. We present the results for $l_{sep} = 20\,\mu$m (solid lines, Fig. S2A-B), 65 μm (dashed lines, Fig. S2C-D), which is the value used for the results presented in the main article (see Table 2 of the main article) and 200 μm (dotted lines, Fig. S2E-F). To study the dynamics, in Fig. S2G we present the pH at the anode/separator interface (left y axis, black lines) and the adsorbed boron, Γ_B, see Eq. 18 in the main article (right y axis, blue lines), both as a function of dimensionless time, t/τ_D.

By comparing the results in Fig. S2A-F we observe small differences between the presented profiles. Accordingly, while comparing the dynamic results in Fig. S2G, only small differences are observed; a slightly increased boron electrosorption was found with a thinner separator.

S2.2. Anode thickness analysis. In Fig. S3 we present characteristic results for different values of the anode thickness, l_A, where we analyze a theoretical cell with the parameters presented in Table 1 and in column 3 of Table 2 of the main article. Fig. S3A, C and E present the profiles of pH (left y axes, black lines) and macropore salt concentration (right y axes, blue lines), and Fig. S3B, D and F present profiles of dimensionless potential, ϕ (left y axes, black lines), and macropore B$^-$ concentration (right y axes, blue lines), all at t/τ_D=2. We present the results for l_A=0.3 mm (solid lines, Fig. S3A-B), 0.6 mm (dashed lines, Fig. S3C-D), which is the value used for the results presented in the main article (see Table 2 of the main article) and 1.2 mm (dotted lines, Fig. S3E-F). To study the dynamics, in Fig. S3G we present the pH at the anode/separator interface (left y axis, black lines) and the adsorbed boron, Γ_B (right y axis, blue lines), both as a function of dimensionless time, t/τ_D.

By comparing the results in Fig. S3A-F we observe some differences between the presented profiles, as the anode thickness affects the salt concentration profiles, resulting in different pH profiles. While comparing the pH at the anode/separator interface in Fig. S3G we observe the highest values of pH ~ 8 at $t/\tau_D = 3$ are developed for l_A=1.2 mm, decreasing with decreasing anode thickness, with pH ~ 7.7 for l_A=0.6 mm and pH ~ 7.5 for l_A=0.3 mm. However, while comparing Γ_B in Fig. S3G, l_A of 0.6 mm presents the best boron electrosorption of $\Gamma_B = 0.15\,\mu$mol/g at t/τ_D=3, where the result for l_A=0.3 mm is $\Gamma_B = 0.104\,\mu$mol/g and $\Gamma_B = 0.098\,\mu$mol/g for l_A=1.2 mm, which are very close. Overall, considering the analyzed conditions, anode thickness of 0.6 mm should be preferred over thinner or thicker anodes.

S2.3. Cathode thickness analysis. In Fig. S4 we present characteristic results for different values of the cathode thickness, l_C, where we analyze a theoretical cell with the parameters presented in Table 1 and in column 3 of Table 2 of the main article. Fig. S4A, C and E present the profiles of pH (left y axes, black lines) and macropore salt concentration (right y axes,

blue lines), and Fig. S4*B, D* and *F* present profiles of dimensionless potential, ϕ (left y axes, black lines), and macropore B^- concentration (right y axes, blue lines), all at $t/\tau_D=2$. We present the results for $l_C=0.3$ mm (solid lines, Fig. S4*A-B*), 0.6 mm (dashed lines, Fig. S4*C-D*), which is the value used for the results presented in the main article (see Table 2 of the main article) and 1.2 mm (dotted lines, Fig. S4*E-F*). To study the dynamics, in Fig. S4*G* we present the pH at the anode/separator interface (left y axis, black lines) and the adsorbed boron, Γ_B (right y axis, blue lines), both as a function of dimensionless time, t/τ_D.

By comparing the results in Fig. S4*A-F* we observe some differences between the presented profiles, where the thickness of high pH region increases with decreasing cathode thickness, see Fig. S4*A, C* and *E*. Therefore, the region of high B^- concentration ($c_{mA,B^-} \geq 0.01$ mM) is thicker for thinner cathodes. Accordingly, in Fig. S4*G* we observe increasing pH at the anode/separator interface and Γ_B with decreasing cathode thickness. Overall, considering the analyzed conditions, a thinner cathode should be preferred.

S3. CDI cell characterization

External electronic resistance (EER), Stern capacitance, and chemical surface charge were experimentally determined from the system and used as fitting parameters in the CDI model. Here we describe the measurement of these parameters.

S3.1. External electronic resistance (EER). We determined EER (Eq. 9 in the main article) of the experimental system from electrochemical impedance spectroscopy using a method based on Hawks et al.(1) We used a two-point configuration, where we connected the cathode to the counter and reference wires and the anode to the working and working sense wires of our potentiostat. During the measurement, 5 mM NaCl solution flowed through the cell at 1 mL/min. We measured the real component of the impedance at 37.7 kHz with 1-4 separator layers, which we took as the series resistance, R_S. Fig. S5 shows a linear fit of series resistance vs. the number of separator layers and yields an EER value of $2.57\,\Omega$ at zero separator thickness, which is displayed in Table 2 in the main article. We note the slope of the best-fit line is the resistance per separator layer, $R_{sep} = 4.16\,\Omega$/separator.

3.2. Equilibrium fittings. To obtain the Stern capacitance, $C_{S,R}$ (Eq. 7 in the main article), we charged and discharged the CDI cell in an-cat configuration to equilibrium ($t_{ch} = t_{dis} = 30\,$min). A solution of 5 mM NaCl flowed through the cell at 1 mL/min (equivalent to Pe=10) in a single-pass configuration. For charging voltages V_{ch} of 0.2 to 1.2 V, in steps of 0.2 V, with a constant discharge voltage $V_{dis} = 0\,$V, we performed five cycles at each V_{ch}. For the fifth cycle, we calculated the Na^+ electrosorption, Γ_{Na^+} via Eq. 18 in the main text, and specific stored charge, q (C/g$_{carbon}$) via

$$q = \frac{\int_{t_{dis}} I\,dt}{m_{an} + m_{cat}}.$$ [1]

In Eq. 1, we note that the current is integrated over the discharge step because parasitic side reactions are negligible at 0 V (which cannot be assumed during the charging step). Thus the integral represents the charge stored capacitively in the electrodes. Assuming identical cathode and anode properties for simplicity, the theoretical Na^+ electrosorption and specific stored charge are

$$\Gamma_{Na^+} = \frac{1}{2}v_{mi}\sum_R \alpha_{mi,R}\left[\left(c_{mi,Na^+,R}^{eq,ch} - c_{mi,Na^+,R}^{eq,dis}\right)_{cat} + \left(c_{mi,Na^+,R}^{eq,ch} - c_{mi,Na^+,R}^{eq,dis}\right)_{an}\right]$$ [2]

$$q = \frac{1}{2}Fv_{mi}\sum_R \alpha_{mi,R}\left|\sigma_{elec,R}^{eq,ch} - \sigma_{elec,R}^{eq,dis}\right|.$$ [3]

In Eqs. 2 and 3, v_{mi} is the electrode specific micropore volume, $\alpha_{mi,R}$ is the fraction of the total micropore volume that is in region R, $c_{mi,Na^+,R}^{eq,ch}$ and $c_{mi,Na^+,R}^{eq,dis}$ are the Na^+ micropore concentration in the R-th micropore region, at the equilibrium charging and discharging states, respectively. Moreover, the subscript of the brackets represents the electrode, where the superscript "cat" represents the cathode and "an" the anode. In Eq. 3, F is the Faraday constant, and $\sigma_{elec,R}^{eq,ch}$ and $\sigma_{elec,R}^{eq,dis}$ are, respectively, the electronic charge densities in the R-th micropore region at the equilibrium charging and discharging states in either the anode or the cathode. By adjusting $C_{S,R}$ to give approximate fits of Eqs. 2 and 3 to the corresponding experimental values for the given range of V_{ch} (the fitting plots are shown in Fig. S6), assuming it is identical in all micropore regions, we experimentally determined a value of $C_{S,R} = 200\,$F/mL, which is also given in Table 2, column 2 in the main article.

3.3. Titrations and chemical surface groups characterization. Here, we characterize the chemical surface groups in the different micropore regions, presented and described in Fig. 5 and the *Theory* section in the main article. To do so, we compare experimental data and theoretical predictions of titration experiments performed to characterize the electrodes. Past theoretical models use the modified-Donnan model to calculate the micropore concentration and relate it to the bulk pH.(2–4) However, here we adapted the model so the micropore concentrations are described using the (ME-)amph-mD model, presented in the *Theory* section of the main article.

We simulate a titration experiment where an electrode, with mass m_e, is immersed in an initial volume, $V_{titration,0}$, of a strong base solution with initial NaOH concentration, c_{NaOH}. During the titration, a volume, $V_{titration}$, of a strong acid with

HCl concentration of c_{HCl} is added, and the solution pH is measured. To calculate the bulk pH, we also seek for the bulk concentration of Na^+, $c_{\text{mA,Na}^+}$, and Cl^-, $c_{\text{mA,Cl}^-}$, so we consider the mass balance of both ions during the titration process,

$$V_{\text{titration,0}}c_{\text{NaOH}} = \left(V_{\text{titration,0}} + V_{\text{titration}} - m_{\text{e}}\nu_{\text{mi}}\right)c_{\text{mA,Na}^+} + m_{\text{e}}\nu_{\text{mi}}\sum_{R}\alpha_{\text{mi},R}c_{\text{mi,Na}^+,R} \qquad [4]$$

$$V_{\text{titration}}c_{\text{HCl}} = \left(V_{\text{titration,0}} + V_{\text{titration}} - m_{\text{e}}\nu_{\text{mi}}\right)c_{\text{mA,Cl}^-} + m_{\text{e}}\nu_{\text{mi}}\sum_{R}\alpha_{\text{mi},R}c_{\text{mi,Cl}^-,R} \qquad [5]$$

where $c_{\text{mi},i,R}$ is the micropore concentration of the i-th ion in region R. To calculate the micropore concentration, we use the Boltzmann equation, $c_{\text{mi},i,R} = c_{\text{mA},i}\exp\left(-z_i\Delta\phi_{\text{D},R}\right)$, where z_i is the ion valence and $\Delta\phi_{\text{D},R}$ is the Donnan potential in region R. We relate $\Delta\phi_{\text{D},R}$ to the other potential drops in the system using the next relation, while setting the reference potential to be the bulk potential, $\phi_{\text{mA}} = 0$, so

$$\Delta\phi_{\text{D},R} + \Delta\phi_{\text{S},R} = \phi_{\text{E}} - \phi_{\text{mA}} = \phi_{\text{E}} \qquad [6]$$

where ϕ_{E} is the electrode potential and $\Delta\phi_{\text{S},R}$ is the Stern potential, found by $\sigma_{\text{elec},R}\cdot F = V_{\text{T}}\cdot C_{\text{S},R}\Delta\phi_{\text{S},R}$, where $V_{\text{T}} \equiv k_{\text{B}}T/e$ is the thermal voltage, where k_{B} is the Boltzmann constant, T is the absolute temperature and e is the elementary charge. Next, we relate the different charge concentrations in the system, where we set the total electronic charge of the electrode to zero,

$$\sum_{R}\alpha_{\text{mi},R}\sigma_{\text{elec},R} = -\sum_{R}\left(\sigma_{\text{chem},R} + \sigma_{\text{ionic},R}\right) = 0 \qquad [7]$$

where the ionic charge concentration in region R is defined by $\sigma_{\text{ionic},R} = \sum_i z_i \cdot c_{\text{mi},i,R}$, and the chemical charge concentration are calculated by $\sigma_{\text{chem,X}} = -c_{\text{chem,X,t}}/\left(1 + c_{\text{mi,H}^+,\text{X}}/K_{\text{X}}\right)$ and $\sigma_{\text{chem,Y}} = c_{\text{chem,Y,t}}/\left(1 + K_{\text{Y}}/c_{\text{mi,H}^+,\text{Y}}\right)$. Lastly, we also consider electroneutrality and water dissociation to hold in the bulk, while assuming water dissociation equilibrium, which is written as

$$c_{\text{mA,Na}^+} - c_{\text{mA,Cl}^-} + c_{\text{mA,H}^+} + \frac{K_{\text{w}}}{c_{\text{mA,H}^+}} = 0 \qquad [8]$$

where K_{w} is the water dissociation constant.

In Fig. S7 we present the data and the fitted model results, from which we determined the values $c_{\text{chem,X}}$=0.80 M, pK_{XH}=4.9, $c_{\text{chem,Y}}$=0.60 M, and pK_{YH^+}=8.5, while using the value $C_{\text{S},R}$=200 F/mL, found in section S3.2. The experimental data is the same as one used for a pristine (as given) electrode presented in previous work.(4)
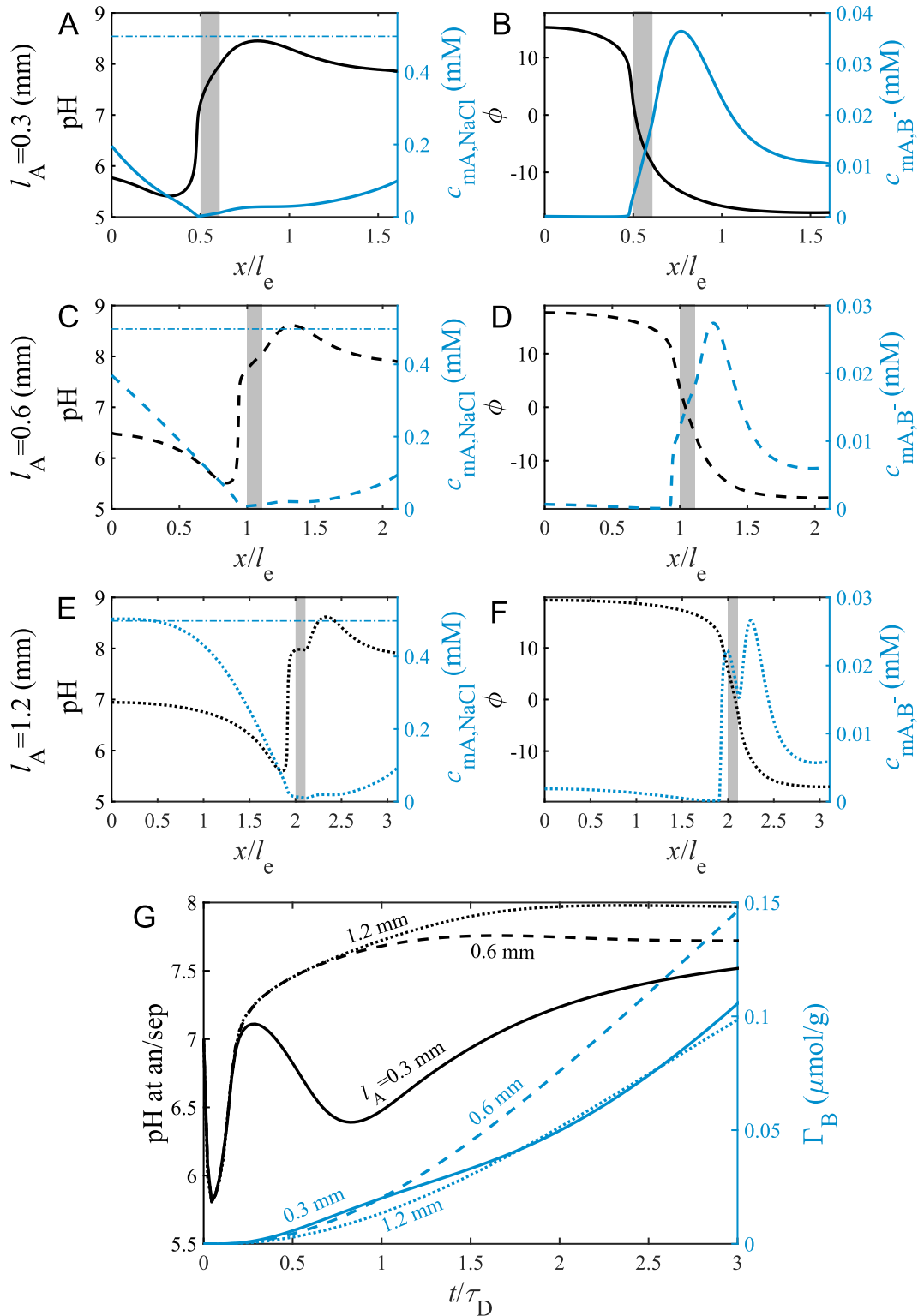
S4. Numerical model

The equations presented in the *Theory* section in the main article were solved using COMSOL multiphysics, which utilizes the finite elements method for the solution of algebraic and partial differential equations. The initial conditions were solved using a stationary study-step, coupling the equations by using a segregated solver, and multifrontal massively parallel sparse direct solver (MUMPS) as the direct solver. The transient equations were solved using a transient study-step, utilizing a fully-coupled solver where the damping factor for the nonlinear method varies between 10^{-18} to 10^{-4}, and the MUMPS solver was used as the direct linear method. Moreover, the maximum element size within the cell is $l_{\text{e}}/300$ and in the reservoirs is $2l_{\text{e}}/15$. Last, the initial time step is $5\cdot 10^{-11}\tau_{\text{D}}$, for $t < 0.02\tau_{\text{D}}$ the maximum step-size is $4.4\cdot 10^{-5}\tau_{\text{D}}$, while for later times the maximum step-size is $0.0044\tau_{\text{D}}$.
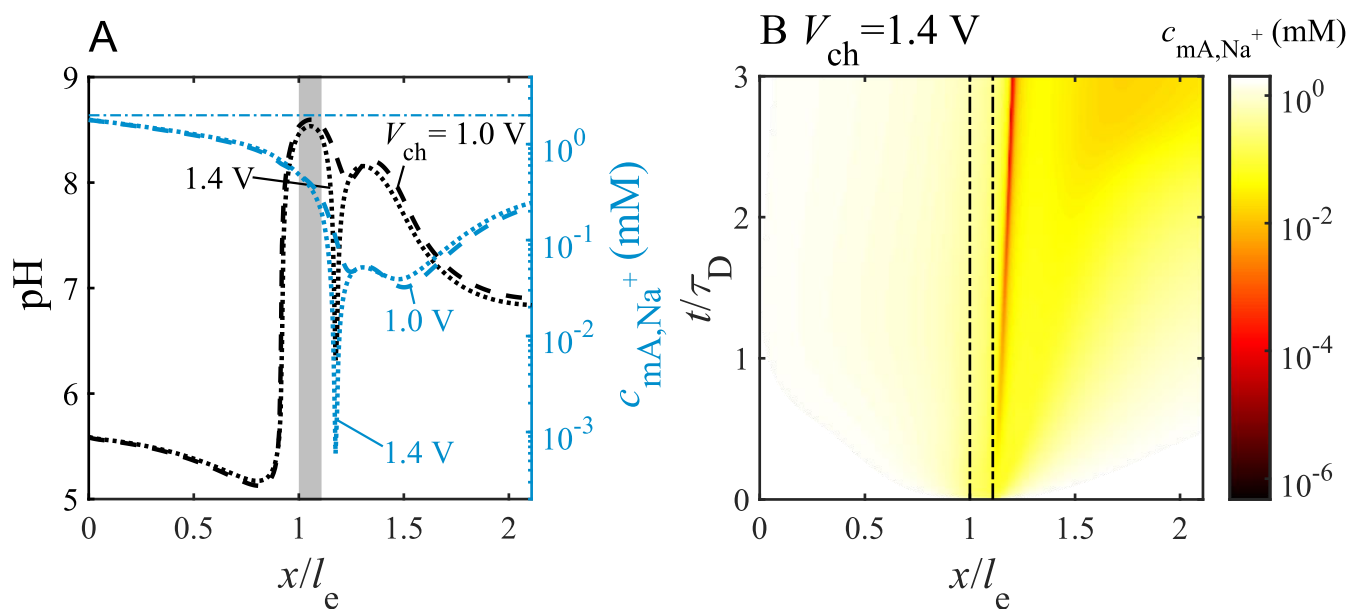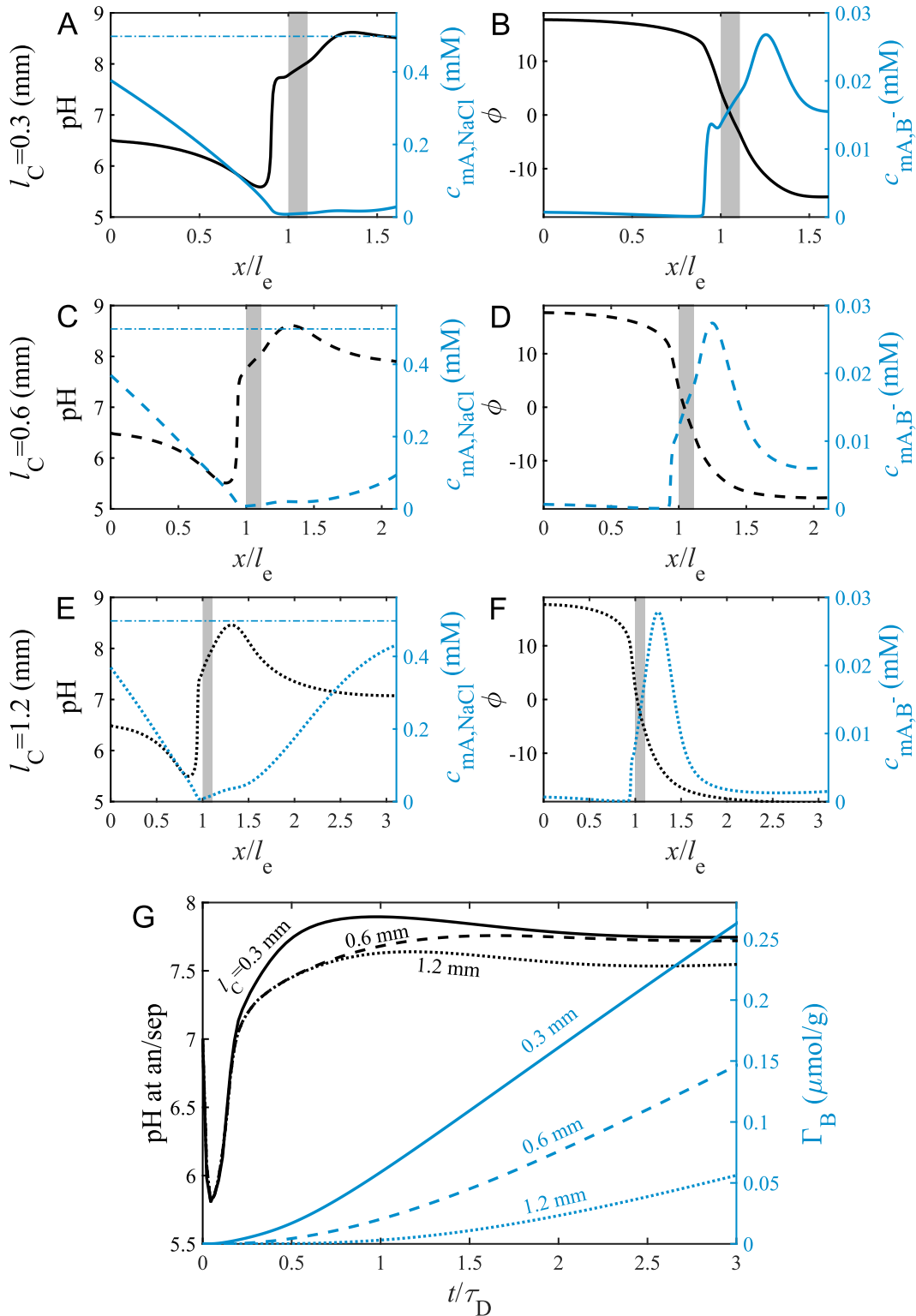
Fig. S1. Extended analysis of pH minima for an FTE CDI cell with feed salt concentration, c_F, of 2 mM, feed boron concentration, $c_{F,B}$, of 0.37 mM and Pe=3. (*A*) Predicted pH (left y axis, black lines) and macropore Na^+ concentration (right y axis, blue lines) profiles for charging voltage, V_{ch}, of 1.0 V (dashed lines) and 1.4 V (dotted lines). The profiles are for $t/\tau_D = 2$, the gray rectangle represents the separator, and the horizontal dash-dotted blue line represents the feed salt concentration. (*B*) Spatiotemporal Na^+ macropore concentration on a logarithmic scale for V_{ch}=1.4 V, where the vertical dash-dotted black lines represent the electrode/separator interfaces.
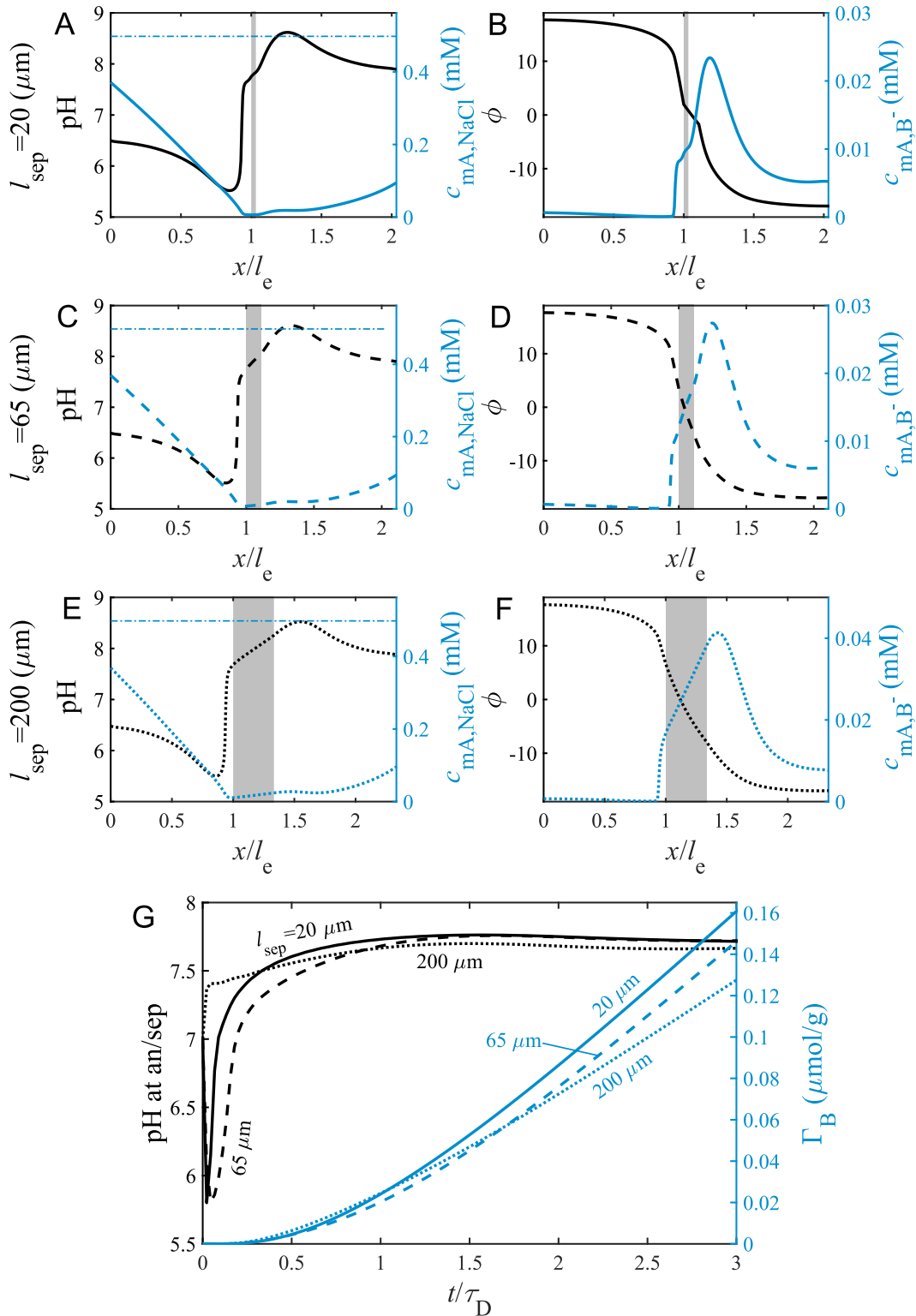
Fig. S2. Effect of separator thickness on pH, macropore salt concentration and potential profiles, and boron removal dynamics. Predictions for an FTE CDI cell with anode and cathode thickness of $l_A = l_C = 0.6\,\text{mm}$, separator thickness of $l_{\text{sep}} = 20\,\mu\text{m}$ (*A, B* and *G*, solid lines), $65\,\mu\text{m}$ (*C, D* and *G*, dashed lines) and $200\,\mu\text{m}$ (*E-G*, dotted lines), all for feed salt concentration, c_F, of 0.5 mM, feed boron concentration, $c_{F,B}$ of 0.37 mM, charging voltage, V_{ch}, of 1.0 V and Pe=1. (*A, C* and *E*) Predicted pH (left y axes, black lines) and macropore salt concentration (right y axes, blue lines) profiles in the FTE CDI cell. (*B, D* and *F*) Predicted dimensionless potential (left y axes, black lines) and B$^-$ macropore concentration (right y axes, blue lines) profiles. The profiles in panels *A-F* are snapshots at $t/\tau_D = 2$, the gray-shaded rectangles represent the separator, and the horizontal dash-dotted blue lines in panels *A, C* and *E* represent the feed salt concentration. (*G*) Predicted pH at the anode/separator interface (left y axis, black lines), and electrosorbed boron (right y axis, blue lines), both as a function of dimensionless time.

Amit N. Shocron, Eric N. Guyes, Huub H.M. Rijnaarts, P.M. Biesheuvel, Matthew E. Suss and Jouke E. Dykstra
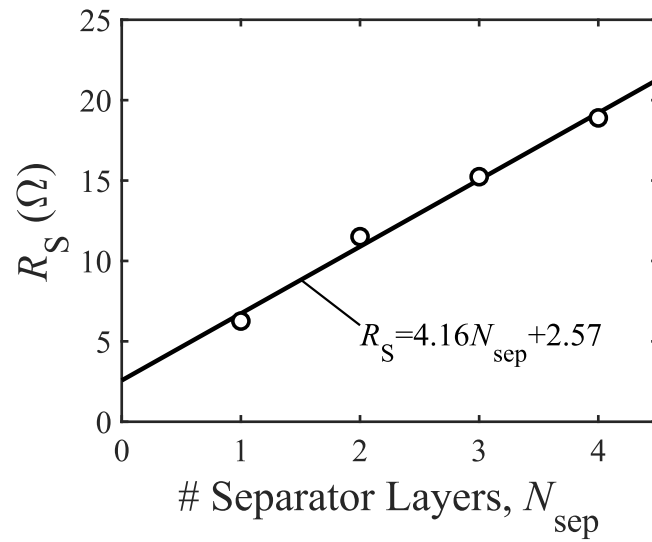
Fig. S3. Effect of anode thickness on pH, macropore salt concentration and potential profiles, and boron removal dynamics. Predictions for an FTE CDI cell with separator thickness of $l_{sep} = 65\,\mu m$, cathode thickness of $l_C = 0.6\,mm$, and anode thickness of $l_A = 0.3\,mm$ (*A, B and G*, solid lines), $0.6\,mm$ (*C, D and G*, dashed lines) and $1.2\,mm$ (*E-G*, dotted lines), all for feed salt concentration, c_F, of $0.5\,mM$, feed boron concentration, $c_{F,B}$ of $0.37\,mM$, charging voltage, V_{ch}, of $1.0\,V$, and Pe=1. (*A, C and E*) Predicted pH (left y axes, black lines) and macropore salt concentration (right y axes, blue lines) profiles in the FTE CDI cell. (*B, D and F*) Predicted dimensionless potential (left y axes, black lines) and B^- macropore concentration (right y axes, blue lines) profiles. The profiles in panels *A-F* are snapshots at $t/\tau_D = 2$, the gray-shaded rectangles represent the separator, and the horizontal dash-dotted blue lines in panels *A, C and E* represent the feed salt concentration. (*G*) Predicted pH at the anode/separator interface (left y axis, black lines), and electrosorbed boron (right y axis, blue lines), both as a function of dimensionless time.

Fig. S4. Effect of cathode thickness on pH, macropore salt concentration and potential profiles, and boron removal dynamics. Predictions for an FTE CDI cell with separator thickness of $l_{sep} = 65\,\mu m$, anode thickness of $l_A = 0.6\,mm$, and cathode thickness of $l_C = 0.3\,mm$ (*A, B* and *G*, solid lines), $0.6\,mm$ (*C, D* and *G*, dashed lines) and $1.2\,mm$ (*E-G*, dotted lines), all for feed salt concentration, c_F, of 0.5 mM, feed boron concentration, $c_{F,B}$ of 0.37 mM, charging voltage, V_{ch}, of 1.0 V, and Pe=1. (*A, C* and *E*) Predicted pH (left y axes, black lines) and macropore salt concentration (right y axes, blue lines) profiles in the FTE CDI cell. (*B, D* and *F*) Predicted dimensionless potential (left y axes, black lines) and B⁻ macropore concentration (right y axes, blue lines) profiles. The profiles in panels *A-F* are snapshots at $t/\tau_D = 2$, the gray-shaded rectangles represent the separator, and the horizontal dash-dotted blue lines in panels *a, c* and *e* represent the feed salt concentration. (*G*) Predicted pH at the anode/separator interface (left y axis, black lines), and electrosorbed boron (right y axis, blue lines), both as a function of dimensionless time.

Amit N. Shocron, Eric N. Guyes, Huub H.M. Rijnaarts, P.M. Biesheuvel, Matthew E. Suss and Jouke E. Dykstra

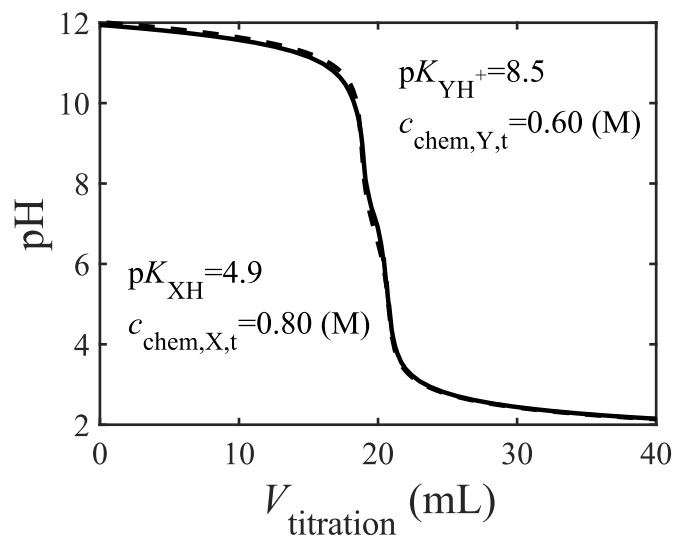**Fig. S5.** Experimental system resistance analysis in 5 mM NaCl solution. Series resistance, R_S as a function of the number of stacked separator layers, N_{sep}. The solid line is the linear fit of the experimental measurements (circles). EER is the vertical intercept of the fitted R_S line at 2.57 Ω, and the slope of the line is the separator resistance, $R_{sep} = 4.16 \ \Omega/\text{separator}$.
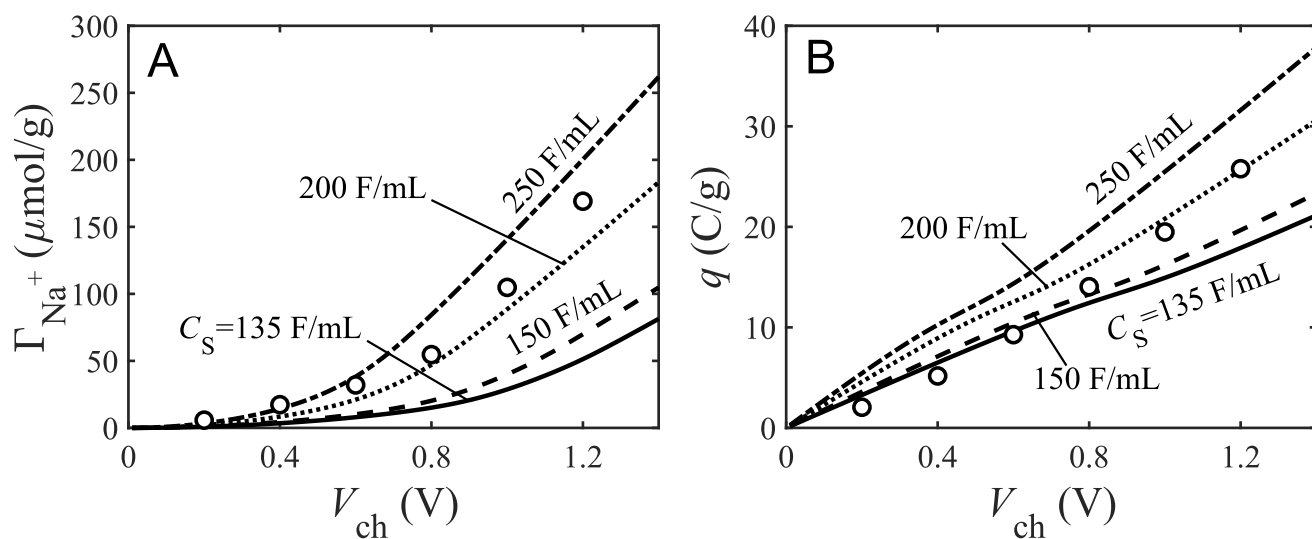
Fig. S6. Stern capacitance fittings based on equilibrium experiments conducted in 5 mM NaCl solution. Experimental measurements (circles) and theoretical predictions for Stern capacitance, C_S of 135 F/mL (solid lines), 150 F/mL (dashed lines), 200 F/mL (dotted lines) and 250 F/mL (dash-dotted lines). (*A*) Adsorbed Na$^+$, $\Gamma_{\text{Na}+}$, and (*B*) stored charge per electrode mass, q, both as a function of charging voltage, V_ch.

Amit N. Shocron, Eric N. Guyes, Huub H.M. Rijnaarts, P.M. Biesheuvel, Matthew E. Suss and Jouke E. Dykstra

Fig. S7. Experimental titration data (solid line) and theory (dased line) for pristine (as given) electrodes. The values of $c_{chem,X,t}$, pK_{XH}, $c_{chem,X,t}$ and pK_{YH+} extracted from for model-to-data fitting.

Table S1. Experimental results.

Electrode order	Pe	Charging voltage (V)	pH_F	Γ_B (μmol/g)
an-cat	1	1.0	6.05	0.093
			7.05	0.100
			7.16	-0.048
			6.71	0.172
an-cat	3	1.0	6.75	0.341
			6.03	0.652
			7.03	0.159
			6.94	0.489
an-cat	5	1.0	6.73	0.504
			6.13	1.18
			7.06	0.339
			7.02	0.225
an-cat	7	1.0	6.18	-0.225
			7.05	-0.386
			7.00	-1.10
			6.62	-0.560
cat-an	1	1.0	5.96	0.004
			6.69	0.020
			6.77	-0.005
cat-an	3	1.0	6.17	-0.411
			6.88	-0.319
			6.26	-0.197
			5.95	-0.079
cat-an	5	1.0	6.27	0.062
			6.90	-0.658
			6.37	-0.224
			5.85	-0.170
cat-an	7	1.0	6.09	-0.259
			6.63	-0.477
			6.79	-0.593
			6.22	-0.204
an-cat	3	0.4	6.04	-0.974
			5.98	-1.04
			5.88	-1.02
an-cat	3	0.6	6.06	-0.301
			6.06	-0.253
			6.12	-0.045
			6.05	-0.502
an-cat	3	0.8	5.99	0.457
			6.12	0.342
			6.09	0.483
			5.99	0.469
an-cat	3	1.2	5.87	0.115
			5.99	0.565
			6.04	0.292
			6.09	0.321

Amit N. Shocron, Eric N. Guyes, Huub H.M. Rijnaarts, P.M. Biesheuvel, Matthew E. Suss and Jouke E. Dykstra

References

1. SA Hawks, et al., Performance metrics for the objective assessment of capacitive deionization systems. *Water Res.* **152**, 126–137 (2019).
2. A Hemmatifar, et al., Equilibria model for pH variations and ion adsorption in capacitive deionization electrodes. *Water Res.* **122**, 387–397 (2017).
3. EN Guyes, T Malka, ME Suss, Enhancing the Ion-Size-Based Selectivity of Capacitive Deionization Electrodes. *Environ. Sci. & Technol.* **53**, 8447–8454 (2019).
4. R Uwayid, NM Seraphim, EN Guyes, D Eisenberg, ME Suss, Characterizing and mitigating the degradation of oxidized cathodes during capacitive deionization cycling. *Carbon* **173**, 1105–1114 (2021).